Materials Science & Engineering A 802 (2021) 140629

Contents lists available at ScienceDirect

Materials Science & Engineering A

journal homepage: http://www.elsevier.com/locate/msea

Solidification microstructure and tensile deformation mechanisms of selective electron beam melted Ni_3Al-based alloy at room and elevated temperatures

Y. Yao [a], C. Xing [a], H. Peng [b,**], H. Guo [b], B. Chen [c,*]

[a] School of Materials Science and Engineering, Beihang University, Beijing, 100191, China
[b] Key Laboratory of High-Temperature Structural Materials & Coatings Technology, Ministry of Industry and Information Technology, Beihang University, 37 Xueyuan Road, Beijing, 100191, China
[c] School of Engineering, University of Leicester, Leicester, LE1 7RH, UK

ARTICLE INFO

Keywords:
Solidification cracking
Grain boundary
Dislocation
Selective electron beam melting
Additive manufacturing
Ni-base superalloys

ABSTRACT

Selective electron beam melting (SEBM) was used to process crack-free Ni_3Al-based IC21 alloy (low density superalloy) containing ~85% γ′-volume fraction. There are distinct differences between dendrites and inter-dendritic regions with the presence of coarse γ+γ′ eutectic and secondary solidification microconstituents (Cr and Mo-rich) in the latter. The pronounced inter-dendritic eutectic regions suggest that a significant elemental partitioning between the liquid and solid occurred during the SEBM. The terminal liquid is trapped at boundaries between dendrites and grains, as evidenced by the liquid films on cracked surfaces. In contrast to extensive studies indicating the segregation of Zr and B, we show unambiguously the segregation of Si to low melting point liquid films and thereby enhancing the susceptibility to solidification cracking in IC21 produced by SEBM. The tensile specimens extracted from the crack-free IC21 samples exhibit superior properties at room temperature (RT) and 1000 °C. The RT deformation mechanism is characterised by cutting γ′-phase with two paired dislocations and antiphase boundaries in between. At 1000 °C tensile deformation, the well-developed γ/γ′ interfacial dislocation networks are in good agreement with their promising high-temperature performance ($\sigma_y = 518 \pm 10$ MPa, $\sigma_{UTS} = 560 \pm 16$ MPa, 20.5% for ductility).

1. Introduction

The intermetallic-based alloys for high-temperature applications have been an active area of research over the past decades. Casting is the only commercially viable approach to process nickel aluminide alloys [1]. Most of the cast Ni_3Al-based alloys have poor weldability, although some success has been achieved to weld them at laboratory level [2]. Ni_3Al-based IC21 alloy, that contains γ′-phase of more than 80 vol% and Re of less than 1.5 wt% (low density), has been developed to manufacture high-pressure turbine guide vanes [3]. This material exhibits excellent high-temperature properties ($\sigma_y = 470$ and $\sigma_{UTS} = 490$ MPa at 1100 °C, creep life of 170.5 h at 140 MPa and 1100 °C). The IC21 alloy with $L1_2$-type superstructure (γ′-phase) falls into the Ni-based superalloy group as it shows the anomalous temperature-dependent yield strength [3,4]. Its predecessor IC6 is considered very susceptible to weld cracking [5].

In fusion welding, superalloys can be categorised as either weldable or non-weldable depending on their Al and Ti contents (γ′-forming elements). The higher Al + Ti contents promote a more rapid γ′-precipitation, and thus γ′-strengthened superalloys are more susceptible to cracking. The adapted weldability diagram from Ref. [6] is shown in Fig. 1, which presents a non-exhaustive summary of superalloys processed by additive manufacturing (AM). It emphasises the non-weldable group but also includes two seminal work on weldable one (i.e. IN718 in Ref. [9,10]). Note that the weldability diagram only accounts for the susceptibility of superalloys to strain-age cracking that occurs during the post-weld heat treatment. Other cracking mechanisms include the solidification [8], liquation [7] and ductility-dip [11] types. The cracked surfaces for both the liquation and solidification types are covered with liquid films [12]. By contrast, ductility-dip cracking occurs

* Corresponding author.,
** Corresponding author.
E-mail addresses: penghui@buaa.edu.cn (H. Peng), bo.chen@leicester.ac.uk (B. Chen).

https://doi.org/10.1016/j.msea.2020.140629
Received 8 October 2020; Received in revised form 1 December 2020; Accepted 1 December 2020
Available online 4 December 2020

at the solid state, characterised with the grain boundary separation [11].

There has been extensive research to understand cracking during selective electron beam melting (SEBM) [13–19] and to heal internal cracks with hot-isostatic-pressing (HIP) [17,20,21]. In SEBM DZ125 work [17], HIP was found to be unsuccessful as the subsequent heat treatment opened up most of the cracks. Also, no success was achieved when HIP was attempted to heal cracks occurring in SLM CM247LC [21]. Selective laser melting abbreviated as SLM is another powder-bed AM. The high build temperature and vacuum environment in the SEBM helps to reduce material cracking due to residual stresses [17,22–24]. This explains the higher number of publications on SEBM non-weldable superalloys compared to SLM, Fig. 1.

A design-of-experiment (DOE) was performed to investigate the crack formation in CMSX-4 processed by SEBM [14] and crack-free samples can be achieved by using low scanning speed and high beam power. Nevertheless, no detailed process parameters were given in Ref. [14], albeit some values mentioned in Ref. [25]. The required line energy to achieve crack-free CMSX-4 was given as 0.6 J/mm, but other process parameters were not specified in Ref. [26]. Crack-free samples in the form of fine columnar, equiaxed grains, and single-crystal have been processed by SEBM in Refs. [15,16,19], but very limited parameters were specified. As pointed out in Ref. [18] that AM parameters are often considered as intellectual property. This means that we still don't have the technical know-how to create crack-free superalloys containing high γ′-volume fraction, let alone Ni_3Al-based alloys. Moreover, the deformation mechanism of SEBM superalloys particularly at high temperature is far from understanding.

The aim of the present work is to obtain crack-free Ni_3Al-based alloy processed by SEBM and elucidate its dislocation deformation behaviour. Dislocation structures at both as-SEBM and tensile deformed conditions were examined using transmission electron microscopy (TEM). Tensile properties at both room temperature (RT) and 1000 °C were evaluated along the build and transverse directions. Ni_3Al-based IC21 alloy with its very high Al content, Fig. 1, represents one of the most difficult-to-weld high-temperature alloys.

2. Experimental

2.1. Material

The IC21 alloy contains 7.6–8.3 Al, 1.5–2.5 Cr, 9.0–12.6 Mo, 0.8–1.5 Re, 2.4–4.0 Ta, and Ni in balance (all in wt.%). Bar stocks were plasma rotating electrode processed (PREP) to obtain IC21 powders. The quality of feedstock powders can affect the SEBM process and the final properties of the build. This warrants the detailed powder characterisation. The round-shaped powders with small amount of satellites can be seen in Fig. 2a. Powder size distribution (PSD) was determined using Bettersize-9300ST laser diffraction method, presented in Fig. 2b, and other key powder properties are summarised in Table 1. Overall, the PREP powders with low porosity content exhibit good flowability and packing density. Analysis of trace elements was performed using inductively coupled plasma atomic emission spectroscopy (ICP-AES), and results are given in Table 1. Elements of B and Zr were strictly controlled at pre-alloying stage as they tended to promote liquid-film related cracking [15,27]. The O content was measured to be 80 ppm by means of inert gas fusion.

2.2. Selective electron beam melting (SEBM)

The SEBM IC21 samples were processed in Arcam A2XX with Control Software 3.2 operating in manual mode. SEBM sample builds per batch consist of 9 rectangular-shaped samples; each with dimensions of 25 × 25 × 30 mm^3 where Z-build direction is along the sample height of 30 mm. Samples were built in vacuum environment (helium-controlled atmosphere) of ~1×10^{-2} mbar on starting plate with dimensions of 100 × 100 × 15 mm^3. The sample support (3 mm in height) was firstly built atop the starting plate, followed by using a high scanning speed to create the low energy density region (3 mm in height). This approach helped to avoid the distortion of the starting plate, even if a very low scanning speed was applied at the later stage.

The build temperature of 1050 °C was achieved by using defocused beam atop each newly raked powder layer at the pre-heat step. This

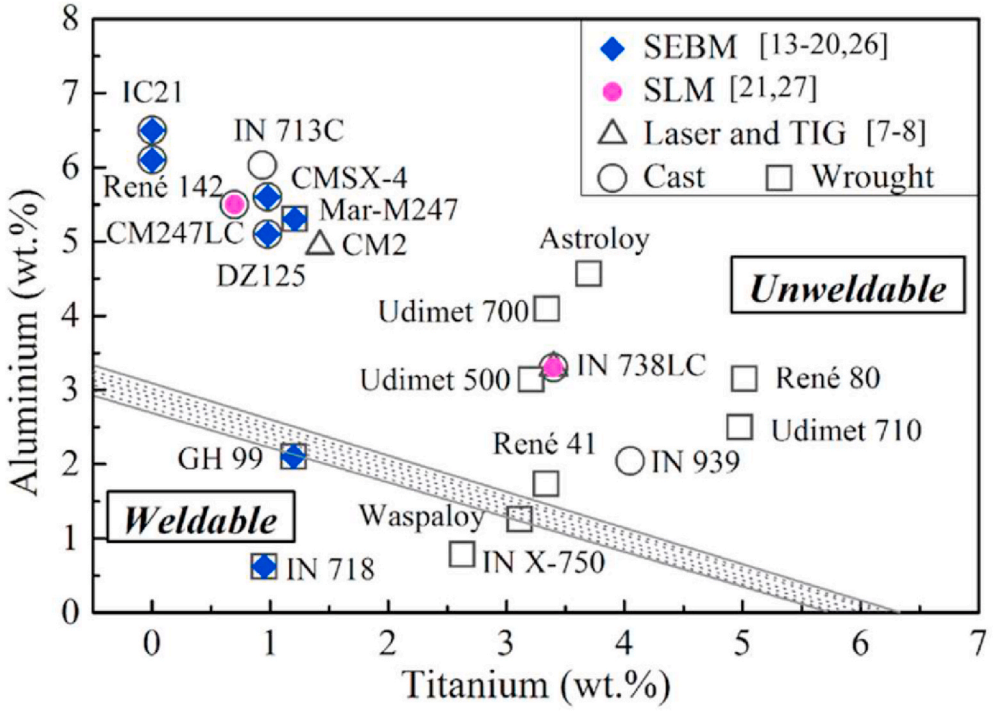

Fig. 1. Effect of Ti and Al on susceptibility to strain-age cracking in Ni-based superalloys. The diagram was adapted from Ref. [6] by including the latest work on SLM/SEBM and crack mechanism studies on laser [7] and tungsten-inert-gas TIG [8] welding.

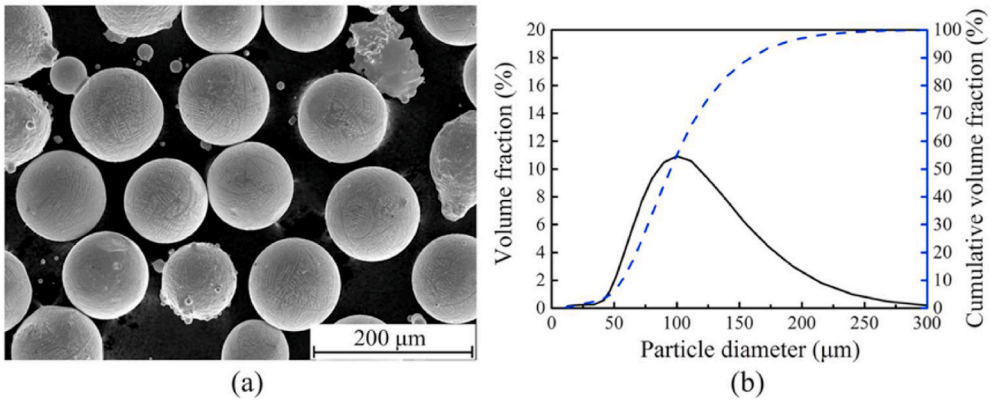

Fig. 2. (a) SEM micrograph of the powder morphology; (b) PSD of PREP powders.

Table 1
Summary of PREP IC21 powder particle properties.

Trace elements, wt.%			Flowability, s	Packing density, g/cm^3	PSD, μm		
Si	B	Zr			D10	D50	D90
<0.01	<0.004	<0.01	14.5	4.80	51.0	85.1	140.0

build temperature has been optimised on the basis of particle sintering experiments, and thereby the pre-heat step can successfully suppress the smoke phenomenon. The build temperature was much lower than the γ′ solvus temperature of 1310 °C as measured by using differential thermal analysis. A layer thickness of 50 μm was used and contour melting was on. More details about the SEBM process can be found in Refs. [17,23,24].

2.3. Design-of-experiment (DOE)

A DOE was performed to study the effects of melt parameters and scan strategies on crack formation in SEBM IC21. The SEBM process window for IC21 alloy was explored by varying beam current (10–20 mA) and scanning speed (v = 150–3800 mm/s) in a wide range. This allowed us to achieve different line energies ranging from 0.16 to 6.67 J/mm. For the high energy input, adjustment of line order (1–237) and line offset (0.1–0.3 mm) was adopted to ensure an even powder bed surface. Line order (LO) is a scan strategy parameter to control the sequence of line-by-line beam scan within one powder layer. When other parameters are kept fixed, the higher LO increases the return time of the adjacent lines, affecting the micro-melt pool morphology and its cooling rate.

During the melt step, beam moves back and forth within one powder layer, referred to as hatching. Fig. 3a illustrates this characteristic beam movement and the distance between each adjacent melt line is defined as line offset L_{off}. When electron beam completes hatching one whole layer, hatch direction is rotated by 90° for consecutive layer. Some typical parameter sets that include specified values of v, L_{off} and LO are summarised in Table 2. These samples were fabricated with the beam current of 10 mA and operating voltage of 60 kV. In general, two

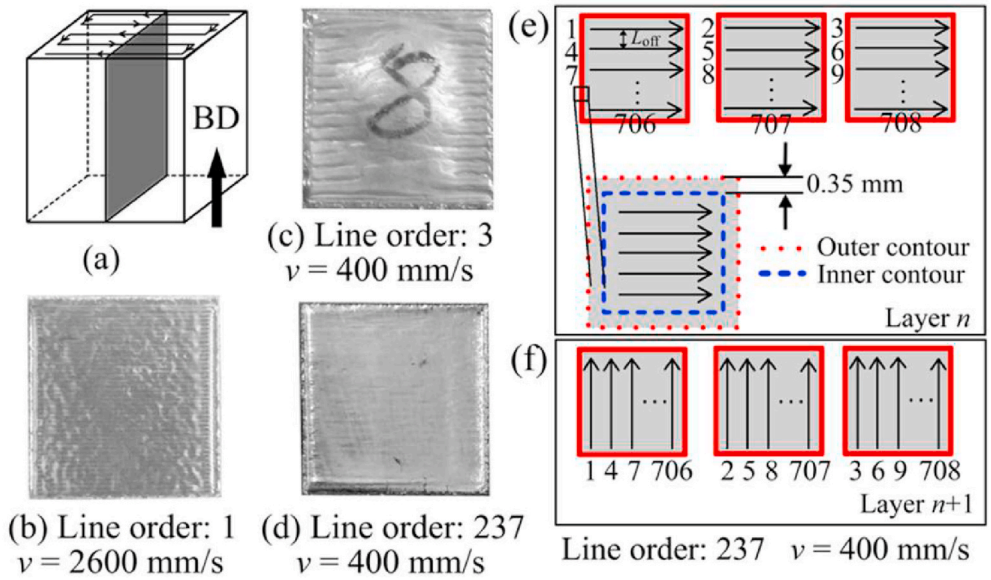

Fig. 3. (a) A schematic showing cross-snake melt strategy; (b) to (d) Photographs of the top surface topology; (e) A schematic of the line scan order for sample E (n layer); (f) n+1 layer with the beam rotation by 90°.

Table 2
Summary of SEBM melt parameters. v: scanning speed; L_{off}: line offset; E_L: line energy.

Sample ID	v (mm/s)	L_{off}	Line order (LO)	E_L (J/mm)	Return time (s)
A	3800	0.1	1	0.16	0.006
B	2600	0.1		0.23	0.009
C	1300	0.2		0.46	0.018
D	700	0.3		0.86	0.034
E	400	0.1	237	1.50	0.295
F	200	0.2	119	3.00	0.590

different scan strategies with lower (LO = 1) and higher LO values (LO = 119, 237) were considered.

By lowering v, the magnitude of energy input as calculated by the line energy ($E_L = P/v$) in Table 2 increased from samples A (0.16 J/mm) to F (3.00 J/mm). As described in Ref. [14], using a high energy input with a low scanning speed helped to obtain the crack-free microstructure. However, for the present IC21 alloy the low value of $v = 400$ mm/s resulted in the formation of wavy top surface, Fig. 3c, owing to the very high energy input [28]. For comparison purpose, another sample that was processed with $v = 2600$ mm/s is shown in Fig. 3b, illustrating a relatively flat top surface. The wavy top surface implies that a significant difference in deposited layer thickness would occur during the SEBM, which often results in insufficient interlayer connection [29]. Furthermore, the very high energy input increases the incidence of evaporating light elements (e.g. Al loss [22,23]).

By using higher LO values, the flat top surface can be realised even with the low v. This was the case for $v = 400$ (LO = 237) and 200 mm/s (LO = 119), Table 2. As illustrated in Fig. 3d, sample E fabricated with $v = 400$ mm/s (LO = 237) exhibited a flat top surface, whereas a wavy top surface was found in the sample processed with the same v but a much lower value of LO = 3, Fig. 3c. The schematic in Fig. 3e shows the hatch pattern sequence when LO = 237 is applied. As outlined by the red colour in Fig. 3e (for clarity only three samples are illustrated), the first and second melt lines were distributed on the first and second sample blocks, respectively. The third melt line became the first melt line on the third sample, and so on. The thickness of contour melt region was 0.7 mm, Fig. 3e, and thus the size of actual region under hatching reduced to 23.6 × 23.6 mm. With $L_{off} = 0.1$ mm, the total number of 236 melt lines were needed per layer, hence 708 melt lines for three samples. The same concept applies to the next layer (n+1 layer), Fig. 3f. In order to keep a constant return time within one layer during hatching, the back-and-forth type beam movement manner was turned off for the high LO-value case. In practice, five individual blocks were treated as one whole build for both the samples E and F, resulting in much greater return time of 0.295 and 0.590 s, Table 2.

2.4. Microstructural characterisation

To investigate the overall crack formation during SEBM, samples A to F (Table 2) were longitudinal cross-sectioned along the build direction, followed by grinding and polishing down to 1 μm. Two individual cross-sectional planes were examined per sample condition and the number density of cracks was evaluated by using the crack ratio method. Scanning electron microscopy (SEM) was performed to reveal liquid films on the cracked surfaces. Both methods were employed previously to elucidate the cracking mechanism [17].

To understand the distribution of cracks in relation to the microstructural features (i.e. grains and dendrites), samples were etched with the chemical solution of 4 g $CuSO_4$ + 5 ml HCl +5 ml H_2O. Metallographic samples were extracted at different Z-height positions, to allow characterising the spatial variations. A Leica DM 4000 optical microscope was used for the grain morphology observation, while SEM was used for revealing the dendritic characteristics.

A Zeiss Supra 55-VP FEGSEM coupled with energy-dispersive X-ray (EDX) was used to study γ/γ' morphology and identify phases. Electrolytic etching was carried out with the chemical solution of 70 ml H_3PO_4 and 30 ml H_2O at 5 V for 4 s, for studying γ'-size variations along Z-build direction. A JEOL JSM7100F FEG-SEM equipped with electron backscatter diffraction (EBSD) detector was used to map crystallographic orientations with a step size of 5 μm. Prior to EBSD, samples were subjected to a careful polishing with colloidal silica. All of the microstructure observations were performed at regions away from the contour melt.

2.5. X-ray photoelectron spectroscopy (XPS)

X-ray photoelectron spectroscopy (XPS) was used to characterise the surface chemistry of liquid films on the cracked surface. To ensure the uncontaminated crack surface to be detected, the crack-containing sample B was machined to dimensions of 20 × 5 × 10 mm^3 with a 2.5 mm deep notch cut. The sample was only fractured to halves prior to the XPS measurement using AXIS Ultra DLD photoelectron spectrometer. A monochromatic AlKα X-ray source with a constant energy of 1486.6 eV was used to irradiate the sample surface with a very shallow depth of <10 nm, resulting in the emission of characteristic photoelectrons.

Ar + ion etching was used to bombard the cracked surface for 90 s at 4.0 keV in vacuum chamber. This resulted in a sputtering rate of ~1.5 nm/min relative to the SiO_2 reference. The material removal rate is consistent with the previous work (1–3 nm/min) [30,31]. Since the thickness of liquid film is typically 2–4 nm [15], it is expected that the sputtering would uncover the solid metal surface beneath the liquid film. Afterwards, XPS spectrum was collected from the same sampling area to provide data comparison.

The survey spectrum was collected with a wide scan of binding energies from 0 to 1200 eV at 1 eV intervals, from which the XPS peaks were identified with the aid of binding energy database [32,33]. XPS spectra were then acquired around the peaks of interest, with much finer intervals of 0.1 eV, to provide chemical state and compositions. The binding energy scales were corrected using C 1s peak at 284.8 eV. Least-squares peak fitting was carried out using CasaXPS [34]. The quantitative data was obtained by dividing the peak intensity (integrated area under the peak) with determined sensitivity factors.

We chose XPS technique, instead of atom probe tomography (APT), to provide statistically significant description of elemental segregations, on a sampling area of 700 × 300 μm. In this context, the XPS data are complementary to those as measured by APT on SEBM [16] and SLM [27] superalloys.

2.6. Mechanical testing and dislocation examination

Vickers micro-hardness (Hv200) at different Z-height positions were performed using FM800 hardness tester and the reported value is the average of 10 measurement points. Tensile tests were performed on SANS CMT 4000 machine equipped with a three-zone furnace and 50 kN load cell. The tests were performed at RT and 1000 ± 1 °C under a constant displacement rate of 0.06 mm/s. Tensile samples with 24 × 3 × 2 mm in dimension were extracted along the Z-build and transverse directions, respectively. Three tensile specimens were tested per condition. The tensile strain was derived using crosshead displacement. Fractography was examined by SEM.

JEOL JEM 2100F field-emission analytical TEM operating at 200 kV was used to characterise the dislocation structure in both as-fabricated and tensile deformed conditions. TEM samples were extracted approx. 3 mm distance to the fracture surface. The γ'-phase identification was aided by the STEM + EDX elemental mapping. All of the detailed dislocation analyses were performed close to the zone axis of [001] or [110], aided by selected area diffraction (SAD). The TEM sample preparation was carried out by twin-jet electro-chemical polishing at −30 °C in a solution containing 10% perchloric acid and 90% ethanol.

3. Results

3.1. Crack formation and mitigation strategy

Fig. 4a–c shows the grain morphology of samples A, B and C, in ascending order of line energy E_L. Fig. 4d–f presents their respective crack morphology. These representative micrographs were taken from the sample height of Z = 15 mm. A high scanning speed of v = 3800 mm/s led to a fine columnar grain structure, Fig. 4a, and the presence of short and discontinuous cracks at grain boundaries can be seen in Fig. 4d. In contrast, with decreasing v, the columnar grains became larger, Fig. 4c, and the intergranular cracks became longer and wider, Fig. 4f.

Quantitative measurements were preformed to reveal the correlation between the grain width and crack ratio, Fig. 5. With the E_L increase, the crack ratio increased initially from 1.52% to 2.06%, accompanied by the grain width increase from 209 ± 67 μm to 515 ± 48 μm. A further increase in E_L, however, led to smaller grain width. The very high E_L was achieved by reducing v in combination with using the appropriate LO; two DOE exemplars with high LO values of 237 and 119 are indicated in Fig. 5. When the grain width reduced to 102 ± 63 μm for sample F, the crack ratio decreased to 0.08%.

The initial increase in grain width as a result of reducing v, Fig. 5, can be attributed to the decreased number of stray grains. A reduced v and higher E_L caused smoother flow of powders and lowered the Marangoni velocity of the micro-melt pool, thus decreasing the convection of broken dendrites [35]. However, a too low v would promote the dendritic fragmentation [9]. This probably explains why there was an inversing phenomenon in Fig. 5.

Fig. 6a presents a large field-of-view (an 18 × 21 mm^2 longitudinal plane) of sample F and it proves that the SEBM process conditions can be optimised to achieve the crack-free IC21 alloy. The stitched optical micrograph in Fig. 6b shows that the columnar grain structure was developed uniformly from the bottom to the top of the build. Fig. 6c showcases the fine columnar grain structure as observed at Z = 16 mm. Quantitative grain width measurements were performed at different Z-height positions. The average grain width was found to be 99 ± 35 μm (Z = 7–11 mm), 101 ± 43 μm (Z = 11–15 mm) and 103 ± 40 μm (Z = 15–19 mm). Thus, the spatial variation of grain width along the Z-direction is judged to be insignificant within the height range of 3–24 mm.

The primary dendrite arm spacing (DAS) at Z = 16 mm was measured as 4 ± 1 μm, Fig. 6d, and no secondary arms can be distinguished. The primary DAS ranged from 3.2 to 4.3 μm along the Z-build direction; hence the spatial variation was insignificant. The measured primary DAS falls into the size range of 3–10 μm as measured in SEBM Inconel 718 [36]. The cooling rate during SEBM solidification was estimated as ~7×10^3 K/s, based on the primary DAS of 4 μm, using the classic equation given in Ref. [37]. The calculated cooling rate is two orders of magnitude lower than that of SLM Hastelloy X having the primary DAS of 0.9–1.2 μm [37].

Fig. S1 summarises the build temperature, vacuum condition, layer build time and sample height as a function of the overall build time for a typical sample build batch. These processing raw data were extracted from the log file to verify the successful fabrication of this very challenging intermetallic-based alloy by SEBM. Fig. S2 depicts how we obtain the crack-free microstructure in the high energy density region. Fig. S3 explains schematically the three sample regions and the post-fabrication examination with respect to the crack formation.

3.2. Identification of liquid films

Cracked surfaces of samples B (E_L = 0.23 J/mm), D (E_L = 0.86) and F (E_L = 3.00) are shown in Fig. 7a–c. It is evident that sample B had continuous liquid films, Fig. 7a. By comparison, sample D fabricated with a higher E_L showed patchy liquid films, Fig. 7b. With the further increase in E_L, sample F exhibited a cleavage-type transgranular fracture, Fig. 7c. Therefore, the presence of liquid films is the cause for cracking in IC21 alloy processed by SEBM.

The same crack investigation method was used to reveal the fractured surface of cast IC21 sample. The presence of cleavage-type fracture can be seen in Fig. 7d. Furthermore, the size of fracture facets in SEBM sample F (crack-free), Fig. 7e, is much smaller compared to that in cast IC21, Fig. 7f. This difference can be attributed to the refined microstructure in SEBM IC21; the primary DAS for the cast IC21 was found to be 500–600 μm, that is two orders of magnitude larger than that in the SEBM counterpart (4 ± 1 μm, Fig. 6d).

3.3. Surface chemistry of liquid films

The cracked surface in sample B with a large area of continuous liquid films, as illustrated by the inset in Fig. 8a, was examined using XPS. The XPS full spectra are presented in Fig. 8a with indexed key characteristic peaks. The elemental compositions in the liquid film are compared with those in the metal matrix, Table 3. Cr and Si were enriched in the liquid film, particularly for the Si content reaching a value of 27.9 wt%. Also, limited segregation of Ta, Re and Hf to the liquid film was found, with respective values of 0.7 at.% (0.03 wt%), 0.2 at.% (0.01 wt%) and 0.05 at.% (0.002 wt%).

The Si enrichment was striking at first glance as the chemical analysis performed on the PREP IC21 powder showed less than 0.01 wt% (Table 1). To ensure the validity of the XPS elemental analysis, the ICP-AES technique was also employed to obtain the bulk composition of Si, Cr, Mo and Al in sample B (Table S1). The Si content was measured to be 0.028 wt% in the bulk, proving that the SEBM process and sample handling were carried out with great carefulness. The ICP-AES results on the bulk sample showed that Cr, Mo and Al were 1.5, 10.2 and 7.9 wt%, respectively. By comparison, the XPS results on the metal matrix showed that Cr, Mo and Al were 7.4, 17.6 and 7.5 wt% (Table 3), respectively. The discrepancy between the ICP-AES and XPS measurements in terms of the Cr and Mo might be due to the micro-segregation, considering the good consistency for the Al content.

The chemical state analysis of Si and Cr was based on the XPS narrow scan spectra. In the case of Si, a single Si(2p) peak exists at the peak position of 102.3 eV for both the liquid film and metal matrix with a clear intensity difference, Fig. 8c. This photoelectron binding energy is in excellent agreement with that for SiO stoichiometry [38]. A unique SiO species does not exist in the solid state, namely it has the composition $Si\text{-}(O)_x(Si)_y$, where the sum of x and y equals to 4 with the most likely composition being x = 2 and y = 2 [39], indicating clusters of Si–Si and Si–O bonds.

In the case of Cr, the chemical state was determined based on the peak-splitting at binding energy of 586.6 eV and 576.9 eV, Fig. 8b. Note that this pair of peaks occurred for both the liquid film and metal matrix. With the aid of the standard spectra for Cr in Ref. [33], it can be known that the chromium oxide Cr_2O_3 has its Cr ($2p_{3/2}$) peak at 576.6 eV together with a distance of 9.7 eV between Cr ($2p_{3/2}$) and Cr ($2p_{1/2}$) characteristic peaks. Thus, the XPS determined Cr-enrichment is most likely to be Cr_2O_3, which also agrees with previous study on chromium-metalloid alloys [40]. By comparison with the liquid film, a pair of characteristic Cr peaks (at 583.5 and 574.2 eV) can be seen in the metal matrix, Fig. 8b. These two Cr peaks represent the Cr–Cr bond, indicating the presence of metallic chromium.

3.4. Grain orientation and inter-dendritic microconstituents

Grain orientation observations along the Z-build direction are presented in Fig. 9, IPF-Z orientation maps. It is evident that with decreasing v, a greater number of grains had their [001] direction aligned more or less with the build direction. The proportion of [001] grains in sample A was estimated as 76.1% by setting the upper limit of the misorientation angle of 15°. This proportion increased to 88.5% for sample D and to 95.1% for the crack-free sample F. The typical fibre texture of SEBM superalloys are widely reported in literature [10,15,

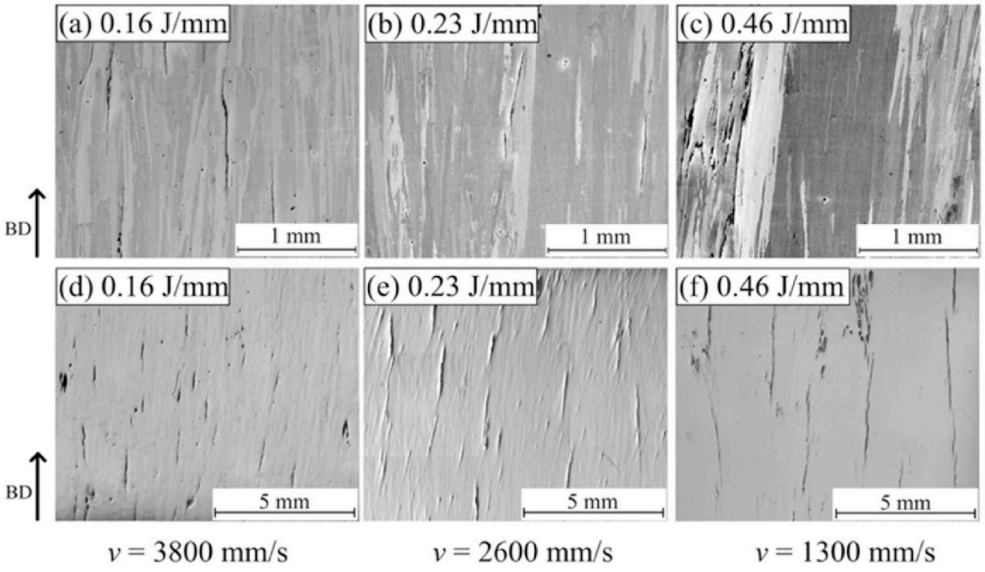

Fig. 4. Optical micrographs of SEBM IC21 samples A to C fabricated with different scanning speed v to achieve a range of line energy E_L: (a) to (c) columnar grain morphology; (d) to (f) crack morphology.

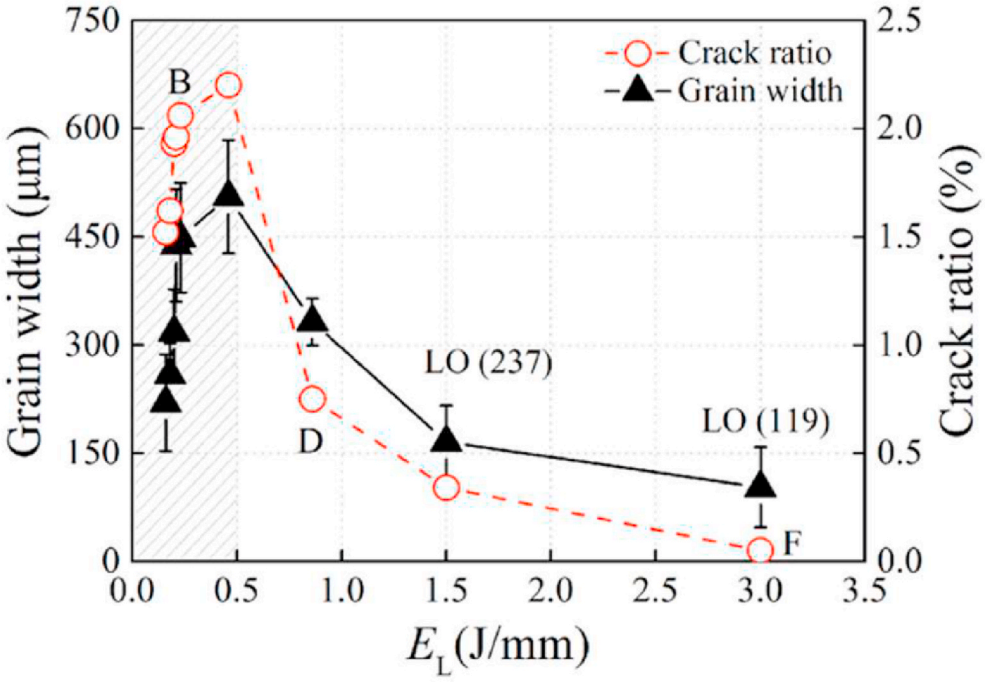

Fig. 5. Relationship between columnar grain width and crack ratio in SEBM IC21 alloy.

17], and this can be attributed to the active grain selection, starting from the micro-melt pool boundary, leading to the growth of grains well aligned with the temperature gradient [9].

SEM observations of γ′-phase in sample F showed size variations from the bottom to the top of the SEBM build. The γ′-size was 300 nm at Z = 16 mm, as measured using the length of the shorter edge, Fig. 10a. The γ′-volume fraction was estimated as 86%, and the γ′-phase coarsening caused γ-channels interconnected. By comparison, the well-defined cuboidal γ′-phase with the average size of 90 ± 10 nm and volume fraction of 84% was found in the sample extracted from Z = 29 mm (i.e. close to the top layers), Fig. 10b. The coarsened γ′-phase close to the bottom of the build had a much lower micro-hardness value, Table 4. For the cast and heat-treated IC21 sample, the γ′-size of 400 nm, volume fraction of 81% (Fig. 10c) and micro-hardness of 443.5 ± 21 were found.

Back-scattered electron SEM images, Fig. 11a–c at different Z-height positions, reveal that secondary solidification microconstituents were formed at the boundaries of dendrites and grains, namely inter-dendritic regions. The needle-shaped phase can be seen in the sample extracted from the middle (Z = 15 mm, Fig. 11b). Such phase was not found at Z = 29 mm, but there was some at Z = 3 mm. The SEM + EDX analysis (the inset of Fig. 11a) shows that both the needle- and round-shaped phases are rich in Mo with 31.3 ± 0.4 wt% and 47.7 ± 1.1 wt%, respectively. By comparison, Mo in the dendrite cores was found to be 8.5 ± 0.3 wt%. By thermal exposing the Z = 29 mm sample at 1000 °C for 2 h, the incipient needle-shaped phase was found (the inset of Fig. 11c). This suggests that

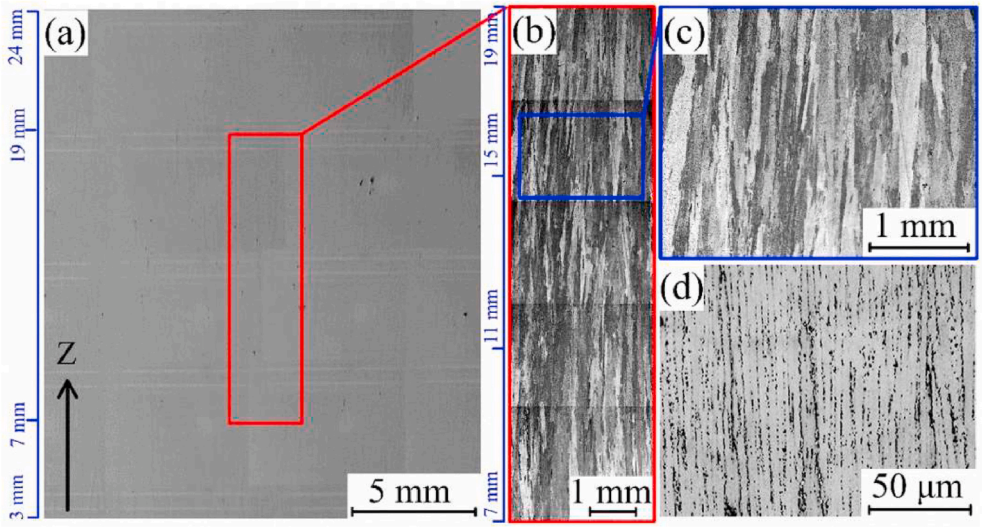

Fig. 6. Optical micrographs of sample F showing the crack-free microstructure in (a) and fine columnar grains in (b); (c) an enlarged view of (b) showing the grain structure; (d) SEM micrograph showing the fine dendritic structure.

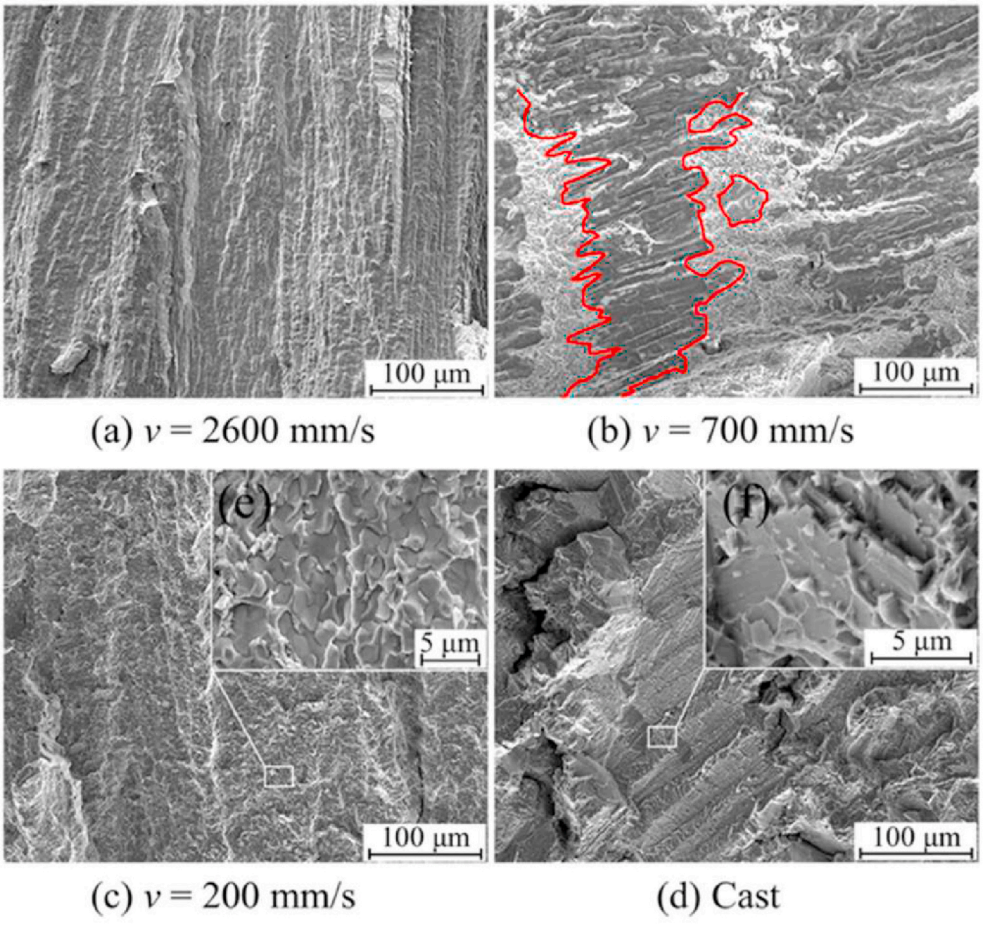

Fig. 7. SEM fractography examination of the cracked surfaces: (a) to (c) SEBM samples B, D and F showing the continuous liquid film, patchy liquid film as highlighted by the red outline, and cleavage-type fracture, respectively; (d) cast IC21 showing cleavage-type fracture; insets (e) and (f) confirm the cleavage-type fracture characteristic. (For interpretation of the references to colour in this figure legend, the reader is referred to the Web version of this article.)

the formation of needle-shaped Mo-rich phase was a result of *in situ* heat treatment during the SEBM fabrication. The limited amount of needle-shaped precipitates at the bottom of the build (Fig. 11a), suggests a dissolution phenomenon, according to Ref. [41].

Darker Z-contrast blocky $\gamma+\gamma'$ eutectic (Cr-enriched: 7.8 ± 0.2 wt%) at inter-dendritic regions, see the inset of Fig. 11b, as opposed to the dendrite core (1.5 ± 0.1 wt% Cr) is also worth mentioning. This indeed agrees with the XPS measurement (Table 3) in terms of revealing some

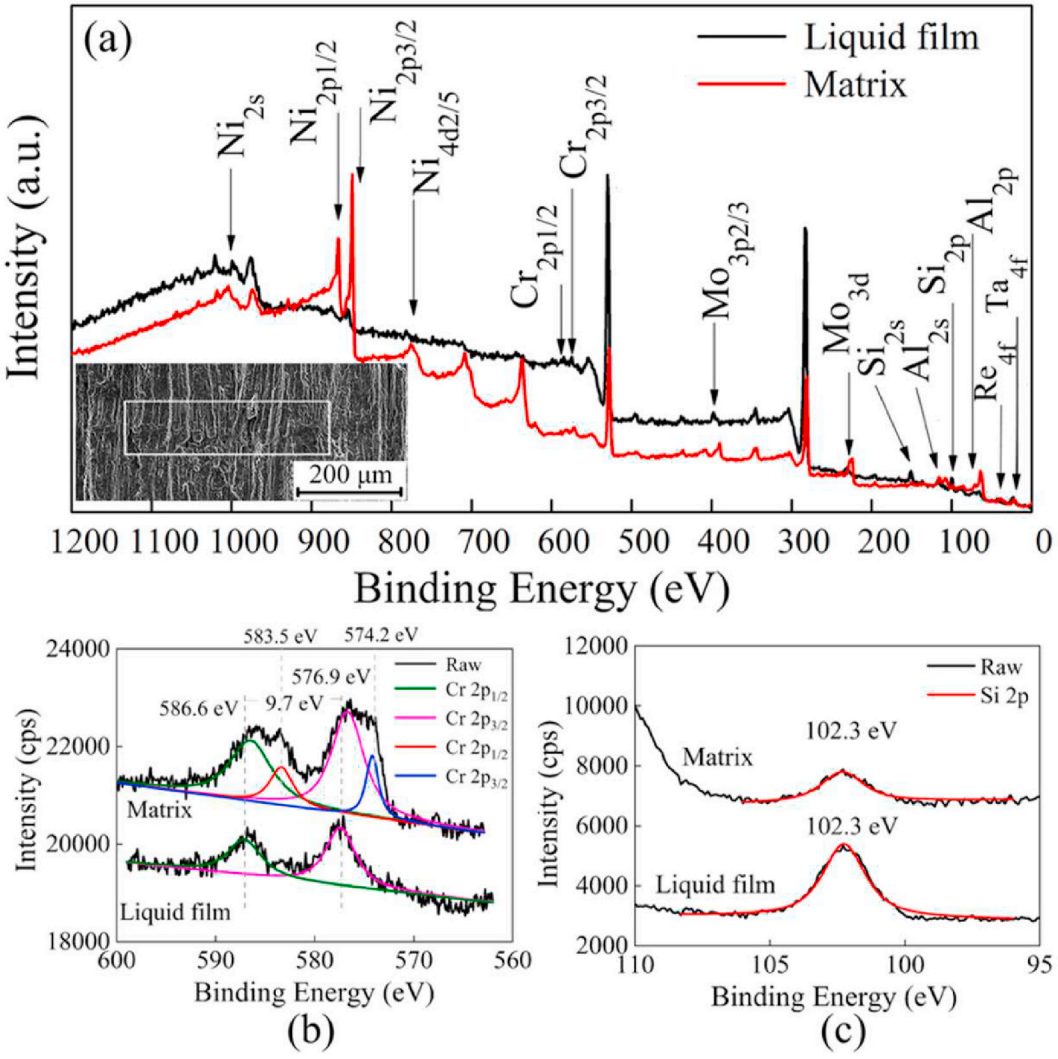

Fig. 8. XPS spectra collected from sample B: (a) wide-range survey spectra and the selected liquid-film analysis area; (b) and (c) narrow-range spectra of Si and Cr.

Table 3
Chemical composition of the liquid film as measured by XPS.

XPS analysed area	Al		Ni		Mo		Cr		Si	
	at.%	wt.%	at.%	wt.%	at.%	wt.%	at.%	wt.%	at.%	wt.%
Liquid film	16.4	10.2	24.4	34.0	5.6	12.7	12.2	15.2	41.4	27.9
Metal matrix	15.6	7.5	60.1	64.2	10.0	17.6	7.7	7.4	6.7	3.4

Cr-enrichment at liquid films. In the study of IC6 laser beam weld [5], low melting point eutectics (consisting of γ+γ′+Ni–Mo phases) were precipitated at the last-stage solidification and they were claimed to be responsible for cracking. For the present SEBM IC21, both the blocky γ+γ′ eutectic and Mo-rich precipitates were found far more frequent at the boundaries. And there was clear evidence for cracking at grain boundaries (e.g. the inset in Fig. 11b).

3.5. Tensile properties

RT and 1000 °C tensile properties for sample F with the crack-free microstructure (Fig. 6a) are summarised in Fig. 12a. The tensile specimens were extracted from the middle of the SEBM build, as shown in the inset of Fig. 12b. The typical stress-strain curves obtained from $BD_{||}$ specimens (along the build direction) are illustrated in Fig. 12b. Compared to the $BD_{\perp}$ (transverse direction), $BD_{||}$ specimens always had higher yield strength (~250 MPa difference) and fracture stress (~500 MPa and ~200 MPa difference for RT and 1000 °C, respectively), Fig. 12a. All specimens were fractured within the gauge section with 0.3–5.1 mm away from the centre. Hence the γ′ microstructural gradient did not cause any abnormal behaviour for the $BD_{||}$ specimens. The elongation-to-fracture of the $BD_{||}$ specimens was measured as 6.0% for RT and 20.5% for 1000 °C, Fig. 12a. It is interesting to note that the $BD_{||}$ specimens at RT exhibited the highest fracture stress together with remarkable strain hardening. Overall, the tensile strength of as-SEBM samples ($BD_{||}$) is comparable to that of cast and heat treated IC21 (σ_y = 554 and σ_{UTS} = 804 MPa at RT, 533 and 585 MPa at 980 °C), although the elongation-to-fracture was inferior (15.2% at RT, 41.5% at 980 °C).

A typical intergranular fracture mode can be found for RT and 1000 °C $BD_{\perp}$ specimens, Fig. 13b and d, respectively, whereas $BD_{||}$ specimens fractured primarily in a transgranular manner, Fig. 13a and c. These fracture characteristics were confirmed based on the high

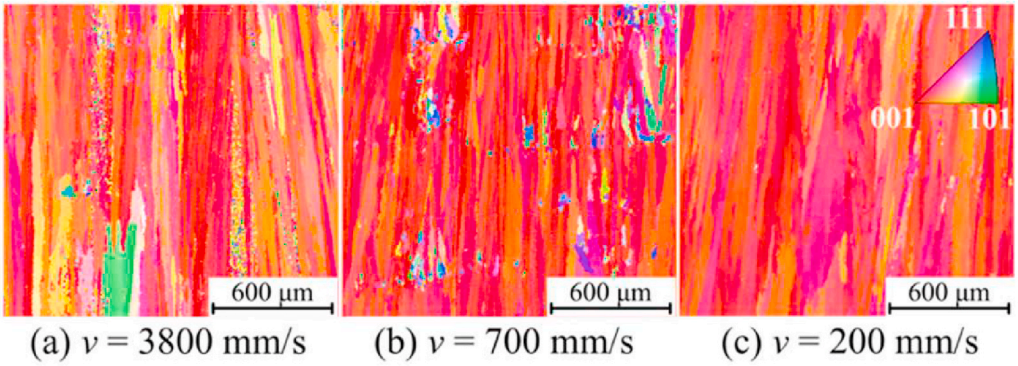

Fig. 9. EBSD-IPF maps of as-SEBM IC21 samples showing the columnar grain structure with their [001] direction parallel to the Z-build direction: (a) to (c) a range of selected scanning speed *v*.

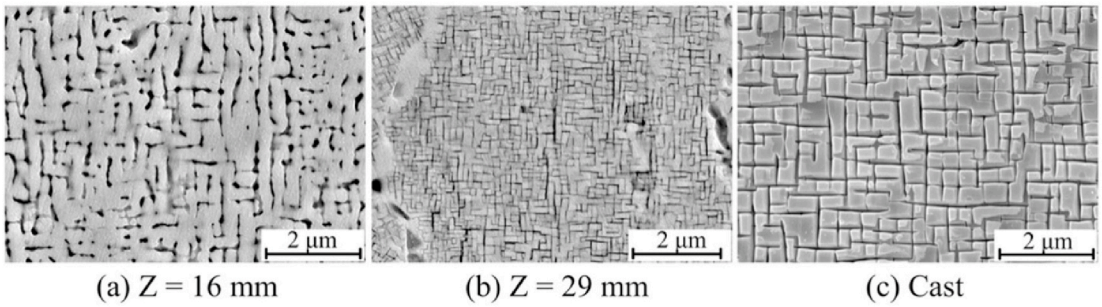

Fig. 10. SEM micrographs of γ′-phase: (a) and (b) SEBM samples extracted from Z-height of 16 mm and 29 mm, respectively; (c) cast and heat treated IC21 sample.

Table 4
Micro-hardness variations along the Z-height for sample F.

Z-height	3 mm	6 mm	11 mm	16 mm	21 mm	29 mm
Hv200	359.5 ± 19	363.5 ± 15	389.5 ± 16	405.7 ± 20	410.0 ± 15	438.3 ± 17

magnification SEM images (Fig. 13e–h). The presence of secondary cracks on the fracture surface in Fig. 13a is a result of grain boundary cracking. By comparison, limited secondary crack was found for the $BD_{||}$ specimen at 1000 °C, Fig. 13c. In terms of the $BD_{\perp}$ specimens, isolated liquid films were revealed for the RT test, Fig. 13b and f, whereas continuous liquid films for the 1000 °C, Fig. 13d and h. Overall, the property discrepancy between the $BD_{||}$ and $BD_{\perp}$ specimens (Fig. 12) can be attributed to grain boundary decohesion.

3.6. Dislocation configurations

TEM observation of dislocation structures in as-SEBM IC21 alloy containing γ′-phase of 86 vol% is shown in Fig. 14a. This TEM micrograph contains both the γ-channel and γ′-phase, as evidenced by the superlattice reflection in SAD. The bright-field TEM image, taken along [110] zone axis, shows extensive misfit dislocation networks at γ-channels and γ/γ′ interfaces, whereas little dislocation was found within the γ′-phase. STEM + EDX analysis of elemental partitioning confirms that the brighter-contrast regions are γ′-phase (not shown for brevity). The irregular-shaped interfacial dislocation networks were associated with the very small dislocation spacing, suggesting a high lattice misfit strain. Due to the high density of tangling, it was impossible to identify the specific nature of these dislocations. The high density of dislocation tangling can also be seen in the γ/γ′ interface region when viewed along the [112] zone axis (Fig. S4).

Note that the formation of interfacial dislocation networks in cast Ni-base superalloy can be triggered during thermal exposure (i.e. without the need of applied stress) [42]. This process was driven by the relaxation of high lattice misfit strain. Of course, the rapid solidification during the SEBM process might further enhance the misfit strain. In this context, the presence of high density of interfacial dislocations in IC21 alloy processed by SEBM is expected.

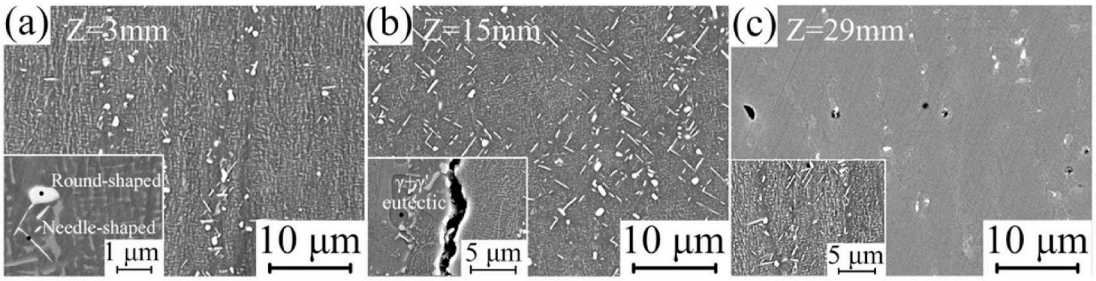

Fig. 11. (a)–(c) Back-scattered electron SEM images of sample B showing the secondary solidification microconstituents; Insets in (a) and (b) showing SEM + EDX analysis areas; Inset in (c) showing thermally exposed SEBM sample.

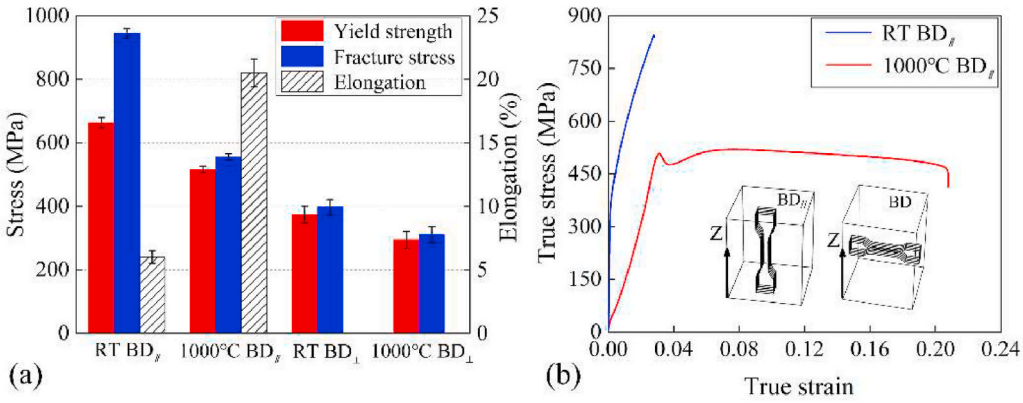

Fig. 12. SEBM IC21 tensile properties at RT and 1000 °C: (a) the average yield strength, fracture stress and elongation-to-failure of $BD_{||}$ and $BD_{\perp}$ specimens; (b) true stress and true strain curves for $BD_{||}$ specimens. Note: the strain was worked out through the crosshead displacement data, and this caused the unrealistic measure of Young's modulus particularly at 1000 °C in (b).

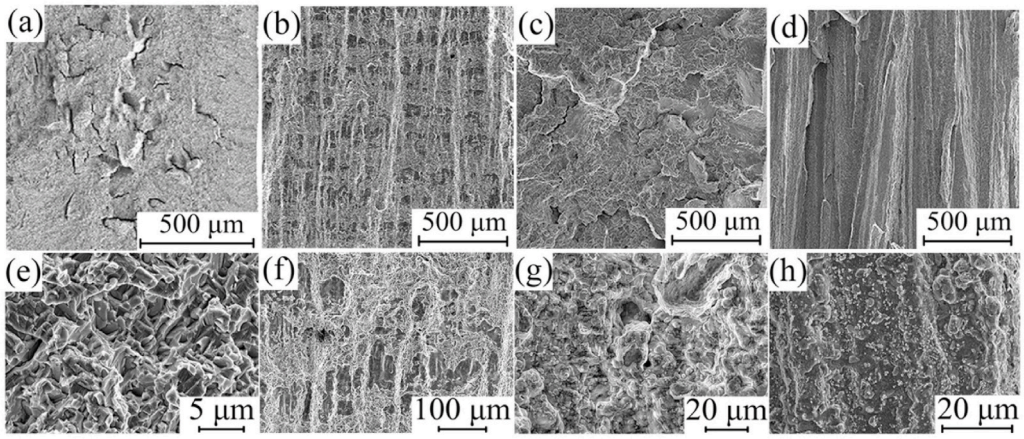

Fig. 13. SEM fractography of tensile specimens: (a) RT, $BD_{||}$; (b) RT, $BD_{\perp}$; (c) 1000 °C, $BD_{||}$; (d) 1000 °C, $BD_{\perp}$. Enlarged SEM micrographs (e) to (h) reveal their fracture characteristics with (e) and (g) indicating the transgranular fracture, while (f) and (h) indicating the intergranular fracture.

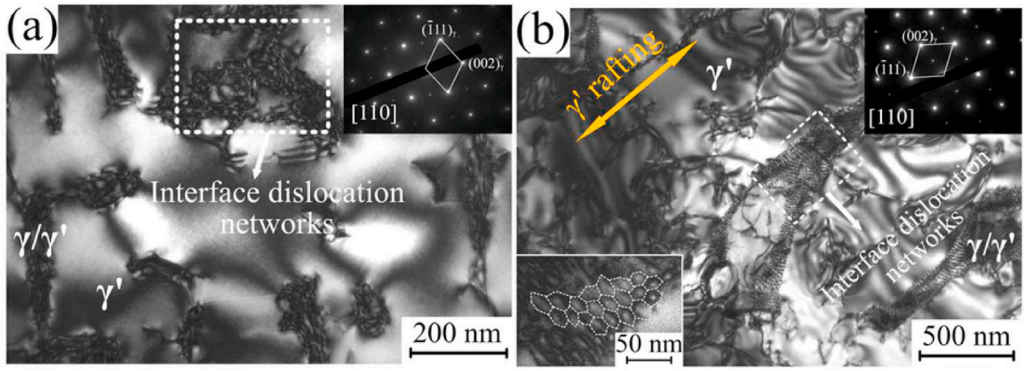

Fig. 14. Interfacial dislocation networks in (a) as-SEBM IC21 sample; (b) after tensile deformation at 1000 °C.

A typical TEM micrograph of the dislocation structure at tensile specimen ($BD_{||}$) at 1000 °C is shown in Fig. 14b. There were well-developed dislocation networks at the γ/γ′ interfaces. Additionally, the γ′-phase started to form plate-like structures, i.e. γ′-rafts with their major axis perpendicular to the far-field applied stress. This process was accompanied by a considerable increase in dislocation densities within the γ′-phase, Fig. 14b. The rafted γ′-phase eliminated a continuous path for dislocations to glide through the matrix, thereby forcing dislocations to shear the γ′-phase for further straining. The enlarged view of the interfacial dislocation networks shows that they were in regular hexagonal shape with a larger dislocation spacing, see the lower left inset in Fig. 14b. This suggests that during 1000 °C tensile straining, interfacial dislocations at the γ/γ′ interfaces as observed in as-SEBM condition (Fig. 14a) were re-arranged to reduce the misfit strain.

The dislocation structure of the RT tensile specimen ($BD_{||}$) was also investigated under TEM. The bright-field TEM image taken along [001] zone axis, Fig. 15a, shows a very high density of dislocations in the γ-channels, γ/γ′ interfaces and γ′-phase. Dislocation density within the

γ′-phase was much lower compared to γ/γ′ interfacial dislocation networks. The STEM + EDX results, Fig. 15b to 15e, confirm that the elemental partitioning in the γ/γ′ microstructure of SEBM IC21 alloy were similar to that as observed in the cast counterpart. Re, Mo and Cr partitioned to the γ-channels as solid-solution strengthening elements, whereas Al was enriched in the γ′-phase.

A typical high magnification TEM image for RT deformed SEBM IC21 is shown in Fig. 16a. The dislocation configurations in Fig. 16a (screw or 60° dislocation segments) are schematically illustrated in Fig. 16b. Two slip dislocation loops on the $(11\bar{1})$ plane within the γ-channel meets at γ/γ′ interfaces, followed by depositing onto the interfaces of (100) and (010). Thereafter, the two dislocation segments at site A[1] would combine to form two superpartial dislocations with the same Burgers vector $\mathbf{b} = a/2\langle 110\rangle$, separated by antiphase boundaries (APB) [40]. This is clearly observed in Fig. 16a, where two dislocations are arranged with the orthogonal relationship when viewed along the [001] direction (Fig. 16b) [43], thus suggesting plastic deformation at RT occurs by cutting through γ′-phase with two paired dislocations and APB in between. The high density of tangled dislocation pairs can be seen within the γ′-phase, see the lower left inset in Fig. 16a. This is consistent with the high strain-hardening rate for the RT deformation (~300 MPa stress increase from yield to fracture, Fig. 12).

4. Discussion

4.1. Elemental partitioning and secondary solidification microconstituents

Ni_3Al-based IC21 alloy was processed by SEBM to achieve fully densified and crack-free microstructure (crack ratio as low as 0.08% in sample F), consisting of the fine columnar grains (~100 μm in width), Figs. 5 and 6, with their [001] direction parallel to the Z-build direction, Fig. 9. The chemical composition of IC21 alloy in the form of powder and SEBM bulk sample F has been measured and there was very limited compositional difference between the two in terms of Al, Cr, Mo, Re, Ta. In detail, Al and Mo increased by 0.1 and 0.2 wt% (Table S1), while both Cr and Ta decreased by 0.1%. This indicates that the Al loss in the present SEBM IC21 alloy was insignificant. The rapid solidification during SEBM promotes the very fine primary DAS (4 ± 1 μm as measured in Fig. 6d). Despite these attractive features, the distinct differences between dendrites and inter-dendritic regions deserve more attention.

The boundaries between grains and dendrites (i.e. inter-dendritic γ+γ′ eutectic) contained a high density of secondary solidification microconstituents, Fig. 11. In particular, grain boundaries were far more frequently decorated by Cr and Mo-rich secondary phases together with the presence of Cr-enriched blocky γ+γ′ eutectic. The γ′-size was much larger within the inter-dendritic region (up to 3 μm, Fig. 11b) in comparison to the dendrite core (90–300 nm, Fig. 10a and b). This means that the high build temperature of 1050 °C cannot remove such pronounced inter-dendritic eutectic regions. Moreover, the high build temperature caused a secondary phase gradient along the Z-build (Figs. 10 and 11).

Previous work [14] showed the presence of inter-dendritic γ+γ′ eutectic (~2 μm in size) in CMSX-4 processed by SEBM. The micro-segregation of refractory elements (Re, W and Ta) on the scale of the primary DAS was claimed to be limited, based on the electron probe X-ray micro-analysis (EPMA). However, they did not comment about the degree of segregation to grain boundaries, nor for inter-dendritic areas. This is expected as the best spatial resolution of the EPMA is about 0.5 μm. Similarly, the SLM Hastelloy X work [37] concluded that no micro-segregation of Ni, Cr, Fe and Si to grain boundaries, based on the SEM + EDX measurement.

In the present study, the observed Cr and Mo-rich secondary phase as well as γ+γ′ eutectic at grain boundaries (Fig. 11) indicate that significant elemental partitioning occurred during the SEBM process. The local compositions at boundaries are consistent with partitioning between liquid and solid phases during solidification if the eutectic liquid is left in these regions [44]. The STEM + EDX results suggest that the segregation behaviour in the γ+γ′ microstructure at dendrite cores is as expected. In particular, Al was enriched in γ′-phase, whereas Mo, Cr and Re partitioned to γ-channels, Fig. 15.

The SEBM IC21 alloy has significant bulk compositional differences from the CM247LC processed by SLM [44], such as Re, Mo, Cr and Al, but the overall elemental partitioning is quite similar despite the different rapid cooling rates between the two AM techniques. For SLM Hastelloy X, the cooling rate was estimated as $\sim 3 \times 10^5$ K/s [37], which is about two orders of magnitude higher than $\sim 7 \times 10^3$ K/s as determined for the SEBM IC21 alloy. Note that the above-mentioned cooling rates were calculated based on the measured primary DAS, and the correlation had been established from the study on a rapidly quenched superalloy [45].

In sum, the presence of secondary solidification microconstituents particularly at boundaries as well as the elemental partitioning in SEBM IC21 alloy indicates that even with the rapid cooling, there is time for significant partitioning of elements between the liquid and solid phases, with eutectic liquid being formed at dendrite and grain boundaries. Segregation in an alloy system is caused by constitutional undercooling during solidification, which is most likely to be the case for the SEBM IC21 alloy. It has been shown that the micro-segregation and precipitation in a highly-alloyed steel processed by SEBM are the same as the conventional means, despite their occurrence in a much finer scale [24].

4.2. Liquid film and solidification cracking

Cracks were exclusively observed to initiate and propagate intergranularly (Fig. 4) and the effect of grain boundary crystallographic misorientation seems to impact the cracking tendency. Sample A with grain size of 209 ± 67 μm and crack ratio of 1.52% was found to have 76.1% of grains within 15° misorientation with respect to [001]-direction (Z-build), Fig. 9a. By contrast, the crack-free sample F (grain size of 102 ± 63), had a higher proportion of grains (95.1%) within 15° misorientation range. Thus, the cracking tendency can be mitigated if the misorientation angle is kept small, namely low-angle grain boundaries (LAGBs) are more resistant to solidification cracking. This result is consistent with the previous study [8] that showed cracking of superalloy single- and bi-crystals increased with the misorientations. Moreover, a clear correlation was identified between cracked grain boundaries and their misorientation angles on an SEBM non-weldable superalloy [15].

The fact that cracks were consistently found at HAGBs does not necessarily mean that the misorientation angle is the sole metallurgical reason for cracking in SEBM IC21 alloy. The presence of liquid films, as revealed on the cracked surfaces in Fig. 7, deserves further attention. The presence of secondary solidification microconstituents at boundaries (blocky γ+γ′ eutectic and Cr and Mo-rich precipitates), Fig. 11, being consistent with XPS determined Cr-rich liquid films, indicates that the progressive enrichment of these elements at boundaries occurred during the repeated solidification and re-melting processes. These low melting point phases can cause the grain boundary segregation induced liquation, a term originated from the welding metallurgy [46]. This term refers to the drop in the solidus caused by the progressive enrichment in solute; thereby expanding the solidification temperature range (STR).

It is worthwhile to mention that the Si-segregated liquid film was not observed in other AM superalloys (e.g. Ref. [16]). By studying the weldability of Haynes HR-160 (a Ni–Co–Cr–Si solid-solution strengthened superalloy) with Si and Fe as variants [47], the amount of inter-dendritic eutectic was found to be proportional to Si content. The non-metallic phase that formed as eutectic, was confirmed by SEM + EDX as the Si-rich G-phase with stoichiometry of $(Ni, Co)_{16}(Ti, Cr)_6(Si)_7$

[1] For the dislocation segments at sites B to D, they form superdislocations in the same manner as described for site A.

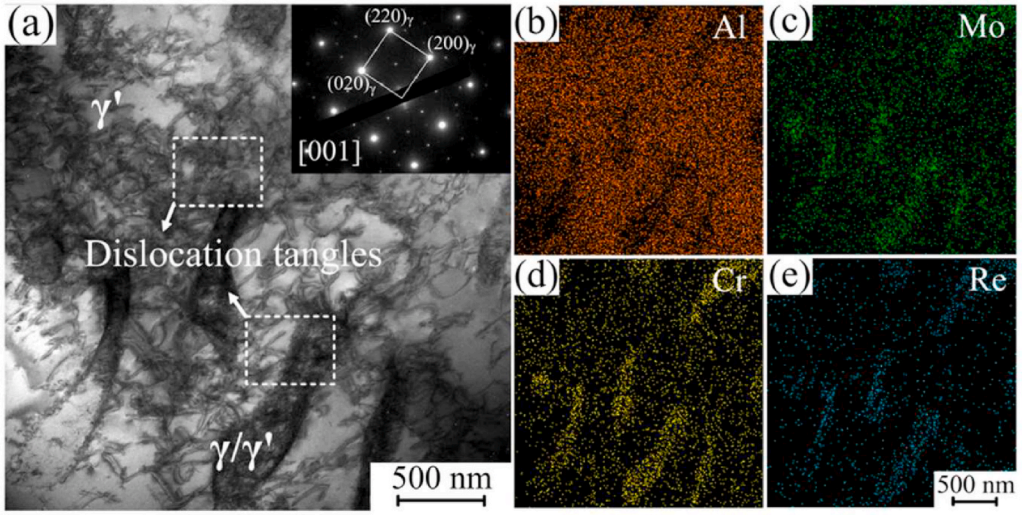

Fig. 15. (a) Bright-field TEM image of RT tensile deformed SEBM alloy IC21, imaged directly along the (001) zone axis; (b) to (e) STEM + EDX elemental mapping.

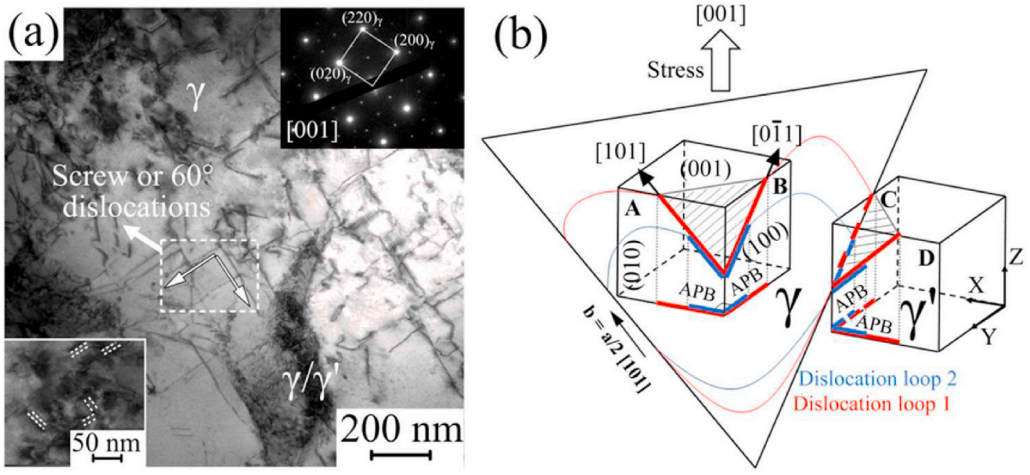

Fig. 16. (a) Dislocation characteristics in γ′-phase after RT tensile deformation showing high density of dislocation pairs and superlattice dislocation segments of *a*/2<110>; (b) Schematic describing the deposition of the screw and 60° dislocation.

[48]. Furthermore, it was commented in Ref. [48] that Si segregated to the solute-rich terminal liquid, which later transformed to γ + G-phase eutectic-type constituent when solidification was completed. From differential thermal analysis on different Si-containing HR-160 alloys [47], it was found that Si caused the STR expansion of the alloy, promoting the low melting point eutectic-phase at grain boundary and inter-dendritic regions. Thus, the detrimental effect of Si to increase the susceptibility to solidification cracking is well known by the cast and weld research community.

Nevertheless, a study on SLM Hastelloy X [37] reached a completely different opinion by emphasising the beneficial effect of Si on crack reduction. They attributed this phenomenon to the rapid solidification of SLM, that helped to trap solutes in the matrix and hence prevented micro-segregation to cracked grain boundaries. The absence of Si segregation at cracked boundaries was based on the SEM + EDX measurement [37]. However, even with a high-end SEM instrument, with the luck of probing a perfectly aligned grain boundary, the spatial resolution of EDX would be 1–2 μm, considering the beam spreading on a bulk sample. In the present work, Si-enrichment at cracked boundaries was revealed by XPS (Fig. 8b) but not detected by SEM + EDX (Fig. 11b), support the above-mentioned technique resolution limitation.

The presence of intergranular liquid films themselves is not sufficient to trigger cracking. Stress would be required to open up the boundaries during the rapid solidification [17,27]. When the remaining inter-dendritic liquid is still in its liquid-film state, together with limited solid bridging of dendritic structures due to liquid wetting [15,18,27], the thermal stresses caused by solidification shrinkage cannot be accommodated by elastic and plastic deformation of the material. The high density of dislocation networks at γ/γ′ interfaces (Fig. 14a) suggests the development of significant thermal stress and misfit stress during rapid solidification. Ultimately, the combined effects of low melting point liquid films and thermal stresses due to successive solidification and re-melting events led to the cracking in SEBM IC21 alloy.

4.3. Tensile properties and microstructure degradation

The RT tensile strength values ($\sigma_y = 672 \pm 22$ and $\sigma_{UTS} = 954 \pm 14$ MPa, Fig. 12) in as-SEBM condition were superior compared to the cast and heat-treated material ($\sigma_y = 554$ and $\sigma_{UTS} = 804$ MPa). The excellent RT tensile properties of SEBM IC21 were consistent with the very fine microstructure and high γ′-volume fraction (Fig. 10). Of course, the property enhancement in SEBM samples should be also attributed to the creation of sufficiently bridged dendrite arms, as implied by the presence of isolated liquid films on the fractured surface of $BD_{\perp}$ specimen,

Fig. 13f.

Compared to the RT tensile results in SEBM CMSX-4 (σ_y = 810 and σ_{UTS} = 910 MPa [26]), the present Ni_3Al-based IC21 alloy exhibited a much higher strain hardening behaviour. TEM observation (Fig. 16) of the γ′-phase shearing, that occurred on multiple {111}<110> glide systems in both the γ and γ′-phase by APB-coupled dislocation pairs, was the dominant RT deformation mechanism. The observed high dislocation densities within γ′-phase (Fig. 15a) and dislocation pairs (Fig. 16a), confirmed that its influence on the motion of dislocations, thereby leading to noticeable strain hardening. The above-mentioned dislocation deformation mechanism has been frequently observed in cast superalloys under large straining [43,49,50].

Another dislocation deformation mechanism associated with the γ′-phase shearing is the so-called {111}<112> slip. This dislocation mechanism is characterised with the formation of superlattice intrinsic stacking faults left at the sheared γ′-phase. TEM studies revealed this dislocation mechanism in cast superalloys during RT tensile deformation [51] and high temperature creep [52,53]. Note that the activation of stacking fault γ′-phase shearing was most often found in stage I and early stage II of creep under the high applied stress. Considering the absence of characteristic feature of {111}<112> slip in all the TEM observations that include both the as-SEBM and tensile deformed conditions, it was less likely that a significant creep deformation occurred during the SEBM process of IC21.

The tensile strength (σ_y = 518 ± 10 MPa and σ_{UTS} = 560 ± 16 MPa at 1000 °C) of the present SEBM IC21 is lower than that of SEBM CMSX-4 (σ_y = 580 and σ_{UTS} = 710 MPa at 950 °C [26]). This could be related to the microstructure degradation caused by high temperature exposure during SEBM process. To understand this side effect better, the microstructure characterisation was performed at different Z-height positions. Several secondary solidification constituents were observed in sample F (crack-free), Fig. 17.

In general, with the prolonged thermal exposure at the high build temperature of 1050 °C (Z = 3 mm, Fig. 17a), the volume fraction of secondary phases and their types increased. Typical secondary phases are indicated in Fig. 17a, including long needle-shaped and short blocky precipitates with the darker phase contrast (Fig. 17d and e), and those having a similar shape but with the brighter phase contrast (Fig. 17f). At Z = 15 mm of Fig. 17b, only a limited number of short blocky precipitates with the darker phase contrast appeared. The volume fraction of precipitates with the brighter phase contrast reduced significantly. At Z = 29 mm (close to the top surface of the SEBM build), Fig. 17c, both the size and volume fraction of the secondary solidification constituents reduced to a low level.

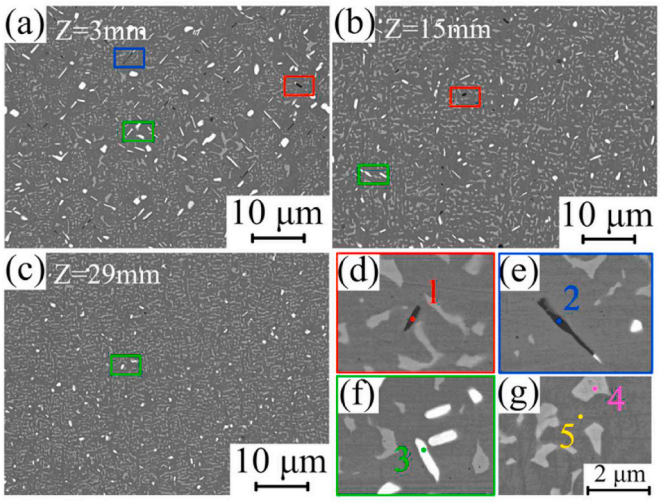

Fig. 17. (a)–(c) Back-scattered electron SEM images of sample F showing the secondary solidification constituents at Z = 3 mm, 15 mm and 29 mm; (d) to (g) Representative SEM images showing the EDX analysis locations.

SEM + EDX phase identification was performed and the average value for each phase is reported in Table 5. The phase (point 5 in Fig. 17g) contained a higher Al of 7.4 ± 0.2 wt% compared to that of point 4 (1.8 ± 0.2 wt%). The Re content in the phase (point 4) was 3.6 ± 0.2 wt% while not detectable in the phase (point 5). Thus, the former is γ-phase while the latter is γ′-phase. The precipitates with the brighter phase contrast (point 3 in Fig. 17f) were found to be Re and Mo-enriched compared to the γ/γ′-phase, whereas the darker contrast precipitates (points 1 and 2 in Fig. 17d and e) were Ta and Cr-enriched. According to the TEM work [54,55], both the darker and brighter precipitates observed in the present IC21 alloy are most likely to be topologically close-packed (TCP) phases. The presence of TCP phases is of particular relevance to the new alloy design tailored for SEBM process. TCP phases are composed of the elements Cr, Mo, Ta and Re (Table 5), and unfortunately this list contains key refractory elements which help to improve the alloy's resistance to creep deformation. Future work to understand the creep and high-temperature fatigue performance is needed for the SEBM IC21 alloy.

5. Conclusions

Solidification microstructure and tensile properties in SEBM Ni_3Al-based IC21 alloy containing ~85% γ′-volume fraction are fully characterised. It can be concluded:

1) The observed inter-dendritic region, consisting of coarse eutectic γ′-phase as well as Cr- and Mo-rich secondary solidification constituents, suggests that strong elemental partitioning occurred during the rapid solidification of SEBM process.
2) The combined effects of low melting point liquid films and thermal stresses due to successive solidification and re-melting events lead to the cracking in SEBM IC21 alloy.
3) Si-segregation and its interaction with other low melting point phase at inter-dendritic regions are important in controlling the susceptibility of SEBM IC21 alloy to solidification cracking.
4) Crack-free IC21 samples can be processed by SEBM with the combined high line order value and low scanning speed, and the tensile properties are comparable with the cast IC21.
5) Plastic deformation at room temperature occurs by cutting through γ′-phase with two paired dislocations and antiphase boundaries in between.
6) At 1000 °C, the SEBM IC21 exhibits excellent properties with σ_y = 518 ± 10 MPa, σ_{UTS} = 560 ± 16 MPa, and 20.5% for ductility, which is consistent with the well-developed γ/γ′ interfacial dislocation networks.

CRediT authorship contribution statement

Y. Yao: Investigation, Formal analysis, Writing - original draft, Visualization. **C. Xing:** Investigation, Formal analysis, Visualization. **H. Peng:** Conceptualization, Supervision, Writing - review & editing,

Table 5
Summary of SEM + EDX chemical composition analyses on secondary solidification constituents in sample F as a function of Z-build height.

Elemental contents in phases (wt.%)				
	1 and 2 (darker contrast)	3 (brighter contrast)	4 (γ-phase)	5 (γ′-phase)
Ni	66.6 ± 3.7	24.1 ± 1.0	73.3 ± 0.4	84.4 ± 0.9
Al	0	0.4 ± 0.2	1.8 ± 0.2	7.4 ± 0.2
Cr	16.4 ± 1.8	0.4 ± 0.1	0	0
Mo	5.4 ± 0.6	48.3 ± 1.6	21.4 ± 1.3	6.4 ± 0.2
Re	0	26.8 ± 3.5	3.6 ± 0.2	0
Ta	11.6 ± 4.2	0	0	0

Funding acquisition. **H. Guo:** Resources. **B. Chen:** Conceptualization, Supervision, Writing - original draft, Writing - review & editing, Funding acquisition.

Declaration of competing interest

The authors declare that they have no known competing financial interests or personal relationships that could have appeared to influence the work reported in this paper.

Acknowledgement

Bo Chen acknowledges financial supports by the UK's Engineering and Physical Sciences Research Council, EPSRC First Grant Scheme EP/P025978/1 and Early Career Fellowship Scheme EP/R043973/1. Hui Peng acknowledges financial support from Key Areas Research and Development Program of Guangdong Province (Programme ID: 2018B090904004).

Appendix A. Supplementary data

Supplementary data to this article can be found online at https://doi.org/10.1016/j.msea.2020.140629.

References

[1] V.K. Sikka, S.C. Deevi, S. Viswanathan, R.W. Swindeman, M.L. Santella, Advances in processing of Ni3Al-based intermetallics and applications, Intermetallics 8 (2000) 1329–1337.
[2] M.L. Santella, Weld solidification cracking in cast Ni3Al alloys, Scripta Mater. 28 (1993) 1305–1310.
[3] H. Zhao, S. Li, Y. Pei, S. Gong, H. Xu, Microstructure and mechanical properties of Ni3Al-based single crystsal alloy IC21, Acta Metall. Sin. 51 (2015) 1279–1287.
[4] R. Kozubski, Long-range order kinetics in Ni3Al-based intermetallic compounds with L12-type superstructure, Prog. Mater. Sci. 41 (1998) 1–59.
[5] R.G. Ding, O.A. Ojo, M.C. Chaturvedi, Fusion zone microstructure of laser beam welded directionally solidified Ni3Al-base alloy IC6, Scripta Mater. 54 (2006) 859–864.
[6] J.N. DuPont, J.C. Lippold, S.D. Kiser, Welding Metallurgy and Weldability of Nickel-Base Alloys, John Wiley & Sons, Inc., New Jersey, 2009.
[7] O.A. Ojo, N.L. Richards, M.C. Chaturvedi, Liquid film migration of constitutionally liquated γ′ in weld heat affected zone (HAZ) of Inconel 738LC superalloy, Scripta Mater. 51 (2004) 141–146.
[8] N. Wang, S. Mokadem, M. Rappaz, W. Kurz, Solidification cracking of superalloy single- and bi-crystals, Acta Mater. 52 (2004) 3173–3182.
[9] H. Helmer, A. Bauereiß, R.F. Singer, C. Körner, Grain structure evolution in Inconel 718 during selective electron beam melting, Mater. Sci. Eng. A. 668 (2016) 180–187.
[10] N. Raghavan, R. Dehoff, S. Pannala, S. Simunovic, M. Kirka, J. Turner, N. Carlson, S.S. Babu, Numerical modeling of heat-transfer and the influence of process parameters on tailoring the grain morphology of IN718 in electron beam additive manufacturing, Acta Mater. 112 (2016) 303–314.
[11] M.G. Collins, A.J. Ramirez, J.C. Lippold, An investigation of ductility-dip cracking in Ni-based weld metals - Part III, Weld. J. 83 (2004) 39s–49s.
[12] S. Kou, Solidification and liquation cracking issues in welding, JOM (J. Occup. Med.) 55 (2003) 37–42.
[13] L.E. Murr, E. Martinez, X.M. Pan, S.M. Gaytan, J.A. Castro, C.A. Terrazas, F. Medina, R.B. Wicker, D.H. Abbott, Microstructures of Rene 142 nickel-based superalloy fabricated by electron beam melting, Acta Mater. 61 (2013) 4289–4296.
[14] M. Ramsperger, R.F. Singer, C. Körner, Microstructure of the nickel-base superalloy CMSX-4 fabricated by selective electron beam melting, Metall. Mater. Trans. 47 (2016) 1469–1480.
[15] E. Chauvet, P. Kontis, E.A. Jägle, B. Gault, D. Raabe, C. Tassin, J.J. Blandin, R. Dendievel, B. Vayre, S. Abed, G. Martin, Hot cracking mechanism affecting a non-weldable Ni-based superalloy produced by selective electron beam melting, Acta Mater. 142 (2018) 82–94.
[16] P. Kontis, E. Chauvet, Z. Peng, J. He, A.K. da Silva, D. Raabe, C. Tassin, J.-J. Blandin, S. Abed, R. Dendievel, B. Gault, G. Martin, Atomic-scale grain boundary engineering to overcome hot-cracking in additively-manufactured superalloys, Acta Mater. 177 (2019) 209–221.
[17] H. Peng, Y. Shi, S. Gong, H. Guo, B. Chen, Microstructure, mechanical properties and cracking behaviour in a nickel-base superalloy fabricated by electron beam melting, Mater. Des. 159 (2018) 155–169.
[18] Y.S. Lee, M.M. Kirka, S. Kim, N. Sridharan, A. Okello, R.R. Dehoff, S.S. Babu, Asymmetric cracking in Mar-M247 alloy builds during electron beam powder bed fusion additive manufacturing, Metall. Mater. Trans. 49 (2018) 5065–5079.
[19] E. Chauvet, C. Tassin, J.J. Blandin, R. Dendievel, G. Martin, Producing Ni-base superalloys single crystal by selective electron beam melting, Scripta Mater. 152 (2018) 15–19.
[20] B. Ruttert, M. Ramsperger, L. Mujica Roncery, I. Lopez-Galilea, C. Korner, W. Theisen, Impact of hot isostatic pressing on microstructures of CMSX-4 Ni-base superalloy fabricated by selective electron beam melting, Mater. Des. 110 (2016) 720–727.
[21] J.H. Boswell, D. Clark, W. Li, M.M. Attallah, Cracking during thermal post-processing of laser powder bed fabricated CM247LC Ni-superalloy, Mater. Des. 174 (2019) 107793.
[22] W. Kan, B. Chen, C. Jin, H. Peng, J. Lin, Microstructure and mechanical properties of a high Nb-TiAl alloy fabricated by electron beam melting, Mater. Des. 160 (2018) 611–623.
[23] W. Kan, B. Chen, H. Peng, Y. Liang, J. Lin, Formation of columnar lamellar colony grain structure in a high Nb-TiAl alloy by electron beam melting, J. Alloys Compd. 809 (2019) 151673.
[24] J. Jin, R. Gao, H. Peng, H. Guo, S. Gong, B. Chen, Rapid solidification microstructure and carbide precipitation behavior in electron beam melted high-speed steel, Metall. Mater. Trans. 51 (2020) 2411–2429.
[25] A.B. Parsa, M. Ramsperger, A. Kostka, C. Somsen, C. Körner, G. Eggeler, Transmission electron microscopy of a CMSX-4 Ni-base superalloy produced by selective electron beam melting, Metals (Basel) 6 (2016) 1–17.
[26] C. Körner, M. Ramsperger, C. Meid, D. Bürger, P. Wollgramm, M. Bartsch, G. Eggeler, Microstructure and mechanical properties of CMSX-4 single crystals prepared by additive manufacturing, Metall. Mater. Trans. 49 (2018) 3781–3792.
[27] M. Cloots, P.J. Uggowitzer, K. Wegener, Investigations on the microstructure and crack formation of IN738LC samples processed by selective laser melting using Gaussian and doughnut profiles, Mater. Des. 89 (2016) 770–784.
[28] H.E. Helmer, C. Körner, R.F. Singer, Additive manufacturing of nickel-based superalloy Inconel 718 by selective electron beam melting: processing window and microstructure, J. Mater. Res. 29 (2014) 1987–1996.
[29] J. Schwerdtfeger, C. Körner, Selective electron beam melting of Ti-48Al-2Nb-2Cr: microstructure and aluminium loss, Intermetallics 49 (2014) 29–35.
[30] S. Oswald, M. Hoffmann, M. Zier, Peak position differences observed during XPS sputter depth profiling of the SEI on lithiated and delithiated carbon-based anode material for Li-ion batteries, Appl. Surf. Sci. 401 (2017) 408–413.
[31] Z.C. Cordero, H.M. Meyer III, P. Nandwana, R.R. Dehoff, Powder bed charging during electron-beam additive manufacturing, Acta Mater. 124 (2017) 437–445.
[32] NIST X-ray photoelectron spectroscopy database, (n.d.). https://doi.org/10.18434/T4T88K, 2019 accessed September 18.
[33] C.D. Wagner, W.M. Riggs, J.F. Davies, Handbook of X-Ray Photoelectron Spectroscopy, Perkin-Elmer Corp., Physical Electronics Division, Eden Praire, Minnesota, 1979.
[34] CasaXPS, Processing software for XPS, AES, SIMS and more, (n.d.). http://www.casaxps.com/ accessed September 10, 2019.
[35] A. Basak, R. Acharya, S. Das, Additive manufacturing of single-crystal superalloy CMSX-4 through scanning laser epitaxy: computational modeling, experimental process development, and process parameter optimization, Metall. Mater. Trans. 47 (2016) 3845–3859.
[36] N. Raghavan, S. Simunovic, R. Dehoff, A. Plootkowski, J. Turner, M. Kirka, S. Babu, Localized melt-scan strategy for site specific control of grain size and primary dendrite arm spacing in electron beam additive manufacturing, Acta Mater. 140 (2017) 375–387.
[37] N.J. Harrison, I. Todd, K. Mumtaz, Reduction of micro-cracking in nickel superalloys processed by selective laser melting: a fundamental alloy design approach, Acta Mater. 94 (2015) 59–68.
[38] M. Anwar, C.A. Hogarth, R. Bulpett, An XPS study of amorphous MoO3/SiO films deposited by co-evaporation, J. Mater. Sci. 25 (1990) 1784–1788.
[39] S.I. Raider, R. Flitsch, J.A. Aboaf, W.A. Pliskin, Surface oxidation of silicon nitride films, J. Electrochem. Soc. 123 (1976) 560–565.
[40] G. Molénat, D. Caillard, Investigations of dislocation mechanisms in Ni3Al at different temperatures: in situ straining experiments in a transmission electron microscope, Philos. Mag. A 69 (1994) 939–959.
[41] C. Xiao, Y. Han, S. Li, D. Wang, J. Song, Q. Li, Effect of Ru on structural stability and mechanical properties of Ni-Al-Mo-B alloy IC6, Mater. Lett. 57 (2003) 3843–3846.
[42] H. Long, H. Wei, Y. Liu, S. Mao, J. Zhang, S. Xiang, Y. Chen, W. Gui, Q. Li, Z. Zhang, X. Han, Effect of lattice misfit on the evolution of the dislocation structure in Ni-based single crystal superalloys during thermal exposure, Acta Mater. 120 (2016) 95–107.
[43] J.X. Zhang, T. Murakumo, Y. Koizumi, T. Kobayashi, H. Harada, Slip geometry of dislocations related to cutting of the gamma' phase in a new generation single-crystal superalloy, Acta Mater. 51 (2003) 5073–5081.
[44] X. Wang, L.N. Cater, B. Pang, M.M. Attallah, M.H. Loretto, Microstructure and yield strength of SLM-fabricated CM247LC Ni-Superalloy, Acta Mater. 128 (2017) 87–95.
[45] H.A. Davies, N. Shohoji, D.H. Warrington, The structure of rapidly quenched nickel-based superalloy ribbons produced by melt spinning, Int. Conf. Rapid Solidif. Process. (1980).
[46] S. Kou, in: Welding Metallurgy, second ed., John Wiley & Sons, Inc., New Jersey, 2003.
[47] I. Maroef, M. Rowe, G. Edwards, The effect of silicon and iron on the weldability of Ni-Co-Cr-Si HR-160® alloy, in: T. Böllinghaus, H. Herold (Eds.), Hot Crack. Phenom. Welds, Springer, Berlin, 2005, pp. 119–140.
[48] J.N. DuPont, J.R. Michael, B.D. Newbury, Welding metallurgy of alloy HR-160, Weld. J. 81 (1999) 408–415.

[49] P.H. Thornton, R.G. Davies, T.L. Johnston, The temperature dependence of the flow stress of the gamma' phase based upon Ni3Al, Met. Trans. 1 (1970) 207–218.
[50] D. Mukherji, H. Gabrisch, W. Chen, H.J. Fecht, R.P. Wahi, Mechanical behaviour and microstructural evolution in the single crystal superalloy SC16, Acta Mater. 45 (1997) 3143–3154.
[51] P. Zhang, Y. Yuan, B. Li, S.W. Guo, G.X. Yang, X.L. Song, Tensile deformation behavior of a new Ni-base superalloy at room temperature, Mater. Sci. Eng. A. 655 (2016) 152–159.
[52] T. Link, M. Feller-kniepmeier, Shear mechanisms of the gamma prime phase in single-crystal superalloys and their relation to creep, Metall. Trans. A. 23 (1992) 99–105.
[53] C.M.F. Rae, R.C. Reed, Primary creep in single crystal superalloys: origins, mechanisms and effects, Acta Mater. 55 (2007) 1067–1081.
[54] C.M.F. Rae, R.C. Reed, The precipitation of topologically close-packed phases in rhenium-containing superalloys, Acta Mater. 49 (2001) 4113–4125.
[55] M.S.A. Karunaratne, C.M.F. Rae, R.C. Reed, On the microstructural instability of an experimental nickel-based single-crystal superalloy, Metall. Mater. Trans. 32 (2001) 2409–2421.